FINAL VERSION

Geo-atmospheric processing of airborne imaging spectrometry data
Part 2: atmospheric / topographic correction

Rudolf Richter
DLR - German Aerospace Center
Remote Sensing Data Center
D - 82234 Wessling / Germany

Daniel Schläpfer
University of Zurich
Remote Sensing Laboratories (RSL)
Winterthurerstr. 190
CH-8057 Zurich / Switzerland

Abstract

A method for the radiometric correction of wide field-of-view airborne imagery has been developed that accounts for the angular dependence of the path radiance and atmospheric transmittance functions to remove atmospheric and topographic effects. The first part of processing is the parametric geocoding of the scene to obtain a geocoded, orthorectified image and the view geometry (scan and azimuth angles) for each pixel as described in part 1 of this jointly submitted paper.

The second part of the processing performs the combined atmospheric/topographic correction. It uses a database of look-up tables of the atmospheric correction functions (path radiance, atmospheric transmittance, direct and diffuse solar flux) calculated with a radiative transfer code. Additionally, the terrain shape obtained from a digital elevation model is taken into account.

The issues of the database size and accuracy requirements are critically discussed. The method supports all common types of imaging airborne optical instruments: panchromatic, multispectral, and hyperspectral, including fore/aft tilt sensors covering the wavelength range 0.35 – 2.55 µm and 8-14 µm. The processor is designed and optimized for imaging spectrometer data. Examples of processing of hyperspectral imagery in flat and rugged terrain are presented. A comparison of ground reflectance measurements with surface reflectance spectra derived from airborne imagery demonstrates that an accuracy of 1 – 3 % reflectance units can be achieved.

1. Introduction

The objective of any radiometric correction of airborne and spaceborne land imagery of optical sensors is the extraction of physical earth surface parameters such as reflectance and temperature. To achieve this goal the influence of the atmosphere, solar illumination, sensor viewing geometry, and terrain information have to be taken into account. An excellent overview on the general prerequisites of radiometric correction was given elsewhere (Duggin and Robinove 1990). A number of papers have been published recently presenting physically-based models for the combined correction of atmospheric/topographic effects (Proy et al. 1989, Sandmeier and Itten 1997, Staenz and Williams 1997, Richter 1998).

Most of the models are restricted to narrow field-of-view sensors, because the scan or view angle dependence of the atmospheric path radiance and transmittance functions is neglected. This contribution includes a full treatment of atmospheric scan angle effects and the topographic influence, includes a processing of thermal bands to derive surface temperature, and has an interface to surface energy-balance models. Although physical models can be quite successful to eliminate atmospheric and topographic effects the following points are of critical importance: (i) an accurate absolute calibration (Slater et al. 1987, Green 1998), (ii) the estimation of atmospheric parameters (Kaufman and Sendra 1988, Gao et al. 1993, Richter 1996, Schläpfer et al. 1998a, Richter and Lüdeker 1999), (iii) the geometric accuracy (part 1 of this paper), and (iv) bidirectional reflectance effects (Kriebel 1978, Kimes 1983, Borel and Gerstl 1994).

Therefore, the radiometric correction of airborne/spaceborne imagery of optical sensors acquired over rugged terrain will remain a challenging task.

2. Airborne Atmospheric and Topographic Correction Model (ATCOR4)

The radiometric correction is based on a geocoded, orthorectified image as described in part 1 of this paper. Part 2 of the processing requires the generation of the atmospheric look-up tables pertaining to the image (flight and solar geometry, range of ground elevations, atmospheric parameters such as aerosol type and optical depth, water vapour, and ozone content), and the resampling with the spectral response function of the sensor channels, (Figure 1). The library of sensors includes DAIS-7915 (Digital Airborne Imaging Spectrometer, Strobl et al. 1996), HyMap (Hyperspectral Mapper, Cocks et al. 1998), AVIRIS (Airborne Visible/Infrared Imaging Spectrometer, Vane et al. 1993), ASAS (Advanced Solid-State Array Spectrometer, Irons et al. 1991) and others.

Put Fig. 1 here

The image-based atmospheric / topographic correction is performed iteratively, as described in the

elements. This is a fairly good approximation for near-nadir viewing geometries (scan angle < 10°) when the solar backscatter region is avoided (Lee and Kaufman 1986). However, many surface covers show anisotropic reflectance behaviour, especially over the large range of view angles that are typically encountered for airborne scanners (30-90° across-track field-of-view). Unfortunately, there is no generally applicable model to account for BRDF (bidirectional reflectance distribution function) effects over land, where a large variety of surface covers exists. Therefore, an interface to scene-dependent models is provided that can be adapted interactively to deal with BRDF effects as described in section 2.2.

In those cases where airborne scenes are available only for one flightline, the restricted number of view angles and the fixed solar geometry often do not allow the retrieval of bidirectional parameters. Thus, the Lambertian assumption has to be used. Usually, there is also no bidirectional reflectance information available from other sources at the typical 1-10 m scale of airborne imagery.

The ATCOR4 model presented here is an extension of the ATCOR3 model for small field-of-view satellite sensors (Richter 1998). Similar to other solutions (e.g., Staenz and Williams 1997) a look-up table (LUT) approach is used for the atmospheric correction employing the Lambertian assumption, since bidirectional surface reflectance models would result in prohibitively large atmospheric databases. The model consists of the major modules called ATLUT, RESLUT and ATCOR4 (Figure 1).

ATLUT calculates geometry-dependent atmospheric LUT's employing the radiative transfer code MODTRAN4 (Berk et al. 1998). ATLUT submits all MODTRAN runs according to user specifications and condenses the MODTRAN output files into much smaller spectral files containing the required minimum spectral information (compare the appendix). All condensed files can be put into a permanent spectral atmospheric database. The size is currently about 2 Gigabytes, a factor 5 smaller than the corresponding MODTRAN database would be. RESLUT resamples the condensed spectral LUT with the band-specific response functions of the selected sensor. ATCOR4 performs the combined atmospheric / topographic correction accounting for the angular and elevation dependence of the atmospheric correction functions and calculates surface reflectance (solar spectral wavelength region) and surface temperature (thermal wavelength region) based on the geocoded and ortho-rectified imagery (see appendix). The special case of a flat terrain is also included.

As shown in the block diagram of Figure 1, model ATCOR4 includes an optional value-adding module that calculates vegetation indices, albedo, leaf area index (LAI), fraction of absorbed photosynthetically active radiation (FPAR), and surface energy balance components such as absorbed solar radiation flux, net radiation, and heat fluxes. Details can be found elsewhere (Richter 2001).

2.1 Considerations for the atmospheric database

The main design drivers of modules ATLUT and RESLUT are the size and the accuracy of the spectral database for the atmospheric correction and the appropriate selection of the options for the radiative transfer (RT) calculations to minimize the computing time without sacrificing the accuracy. The size of the ATLUT output files is minimized compared to the standard MODTRAN output by including only the

direct and diffuse flux, and spherical albedo. Further considerations are the selection of the scan angle increment to keep interpolation errors small, the spectral resolution, and the number of streams for the multiple scattering calculations. These items are discussed now. More details are given in Richter (2000b). The advantage of the database is the possible repeated use of the results of radiative transfer calculations requiring only a resampling with the sensor-specific response functions.

For the solar region, MODTRAN's DISORT option (discrete ordinate radiative transfer, Stamnes et al. 1988) with 8 streams is used as default at a spectral resolution of 15 cm^{-1} . Tests were run with 16 streams also, but results were close to the 8-stream results for scan angles smaller than 60° and solar zenith angles smaller than 70°. However, Isaacs 2-stream option (Isaacs et al. 1987) can also be selected by the user for a faster, but less accurate, processing. The spectral resolution is selected at 15 cm^{-1} in the wavelength range 0.35-1.8 µm. A 1 cm^{-1} grid averaged to 4 cm^{-1} is employed in the 1.8 – 2.55 µm range to improve the spectral resolution to about 2 nm in the short-wave region. In the thermal region a 2-stream RT calculation is sufficient. Here, the highest spectral sampling of MODTRAN (1 cm^{-1}) is employed, which is equivalent to a 10 nm sampling distance at the wavelength of 10 µm.

Those calculations intended for permanent use in the database are performed for a large swath angle (typically ±40° with respect to nadir) comprising the spectral regions of 0.35-2.55 µm and 8-14 µm. The scan angle range and spectral regions cover the need for most earth observing multispectral / hyperspectral sensors (Vane et al. 1993, Cocks et al. 1998, Strobl et al. 1996, Gower et al. 1992). The 3-5 µm atmospheric window region is currently not included, because the separation of reflected solar and emitted thermal radiation is difficult and requires multispectral channels (Wan and Li 1997). For the DAIS instrument mentioned in the library of sensors in Figure 1, the multispectral condition cannot be met, because it has only one channel in this wavelength region.

The scan angle increment should be large on the one hand to reduce the number of RT calculations, but it should be small to keep any scan angle interpolation errors small. As a compromise, the recommended scan angle increment is carefully selected at 5° to keep the relative interpolation error in the at-sensor radiance smaller than 1 % for scan angles up to 40° (Figure 2). However, calculations can also be defined for a smaller swath angle, e.g. 10°, to reduce the time for the LUT calculation. For cases where a digital elevation model is employed the elevation range (minimum, maximum) and elevation increment have to be specified by the user. RT calculations are then performed for the discrete set of selected elevations and scan angles. A special nomenclature is used for the condensed spectral MODTRAN files and the "*.atm" files (resampled with sensor-specific spectral response curves) to facilitate documentation and database access (Richter 2000a).

Put Fig. 2 here

Most airborne imaging instruments do not have a tilt capability. Some instruments record images for a number of tilt angles. The following types of sensor geometry (labeled A, B, C) are supported comprising the majority of the known airborne scanners: *Type A are* instruments without tilt capability having $n \geq 1$

and the solar azimuth) and scan angle change from the left to the right part of the scanline. This is taken into account for the radiative transfer calculations. If the relative azimuth angle for the right part of the scanline is ■, then it is 180°- ■ for the left part. *Type B* are along-track tilt instruments with the number of tilt angles equal to the number of spectral bands, e.g., MOMS-02 (Modular Optoelectronic Scanner, Kaufmann et al. 1989, Richter and Lehmann 1989), and HRSC (High Resolution Stereo Camera, Hauber et al. 1996). The relative azimuth angle ■ changes with pixel position in a scanline and with tilt angle. *Type C* are along-track tilt instruments with m > 1 bands per tilt angle, e.g., ASAS (Irons et al. 1991) , and MISR (Multi-angle Imaging Spectroradiometer, Diner et al. 1991). Again, the relative azimuth angle changes with pixel position and tilt angle. Since the band index in model ATCOR4 corresponds to a wavelength index, each tilt angle has to be treated as a separate sensor in this context.

2.2 Interface to bidirectional reflectance (BRDF) models

It is well known that many surface covers show BRDF effects (Kriebel 1978, Kimes 1983). However, there is no generally applicable model for all land scenarios. Most BRDF models are empirical or semi-empirical models where three or four parameters have to be fitted depending on surface cover, available view and illumination geometries (Roujean et al. 1992, Wu et al. 1995, Wanner et al. 1995 and 1997, Hu et al. 1997) and physical parameters (leaf are index or vegetation index). Specialized scene-specific evaluations are possible depending on the available number of solar and viewing geometries. Therefore, an interface to BRDF models is presented here that is implemented within the models PARGE and ATCOR4 (Figure 3). ATCOR4 first performs the atmospheric/topographic correction based on the assumption of Lambertian surface elements (see appendix).

The SPECL code performs a spectral pre-classification of the reflectance cube based upon template spectra at the Landsat Thematic Mapper reference wavelengths (i.e., 0.48, 0.56, 0.66, 0.83, 1.6, 2.2 µm) and returns a map of class indices for each pixel. The template spectra consist of typical vegetation covers, soil, sand, and water taken from literature (Bowker et al. 1985, Vermote et al. 1997). If the spectral reflectance signature agrees within a 10% margin at the reference wavelengths with one of the class template spectra it is put into this class, otherwise it belongs to the class *undefined* (Richter 2000a). For each pixel of a certain class the viewing and solar geometry is known. Depending on the available range of angles, a 3- or 4-parameter fit (denoted symbolically with $\alpha_i, \beta_i, \gamma_i$ in Figure 3) can be applied with a user-defined BRDF model. The user has access to the class map, the reflectance cube(s), DEM files (elevation, slope, aspect) and to the view angle file from PARGE (scan and azimuth angle for each pixel).

Figure 3 shows the two options that are the output of any BRDF model : the transformation of off-nadir reflectance values into nadir values, and the calculation of albedo values, i.e., bihemispherical reflectances. Details with example scenes acquired in the solar principal plane are beyond the scope of this paper and will be presented in a forthcoming paper.

Put Fig. 3 here

2.3 Impact of geometric resampling

Since geocoded imagery is used as input to the atmospheric correction, the selected geometric resampling algorithm has some implications on the radiometry and, subsequently, on the surface reflectance / temperature calculation. For geocoding in a flat terrain, the nearest neighbour approach is recommended to retain the original radiometry, if image-derived surface reflectance / temperature data have to be compared with ground measurements on a pixel-by–pixel basis. However, this requires the consideration of the airborne sensor's modulation transfer function and is seldom performed. Usually, ground measurements are conducted in large homogeneous fields and image pixels are averaged (at least 3 x 3 pixels) to enable a statistical evaluation for the comparison (Slater et al. 1987, Green 1992, Santer et al. 1992, Richter 1997). Then, the difference between bilinear and nearest neighbour resampling of the spatially uniform averaged data is much smaller than the standard deviation of the ground measurements in most cases or even within the noise level of the instrument, and the choice of the resampling technique does not matter. Large differences between both methods do occur at field boundaries with high brightness contrast. Then, the corresponding relative reflectance differences can range up to 100% or more. Additional information on geometric resampling is given in part 1 of this joint paper.

For ortho-rectified imagery the same arguments apply. In addition, the radiometric integrity critically depends on the spatial resolution and accuracy of the DEM as discussed in section 4.

Another aspect concerns spatial gaps in the original data. These are caused by missing scan lines or aircraft movements. During the geocoding process these gaps have to be filled and bilinear interpolation is an appropriate algorithm to obtain smooth transitions and a visually improved appearance.

3. Sample cases

Two cases of hyperspectral image processing will be presented here, the atmospheric correction for a scene in flat terrain and the combined atmospheric / topographic correction for a scene in rugged terrain. The second example intentionally presents imagery acquired under non-ideal conditions, i.e., GPS clock information was partially missing and the spatial resolution of the DEM is coarser than the sensor's footprint. However, this is a typical "*real-world*" situation encountered in many cases. It leads to a reduced accuracy of the geo-atmospheric processing, but still yields satisfactory results.

3.1 HyMap imagery of Barrax, Spain, flat terrain

As an example of processing a hyperspectral scene over flat terrain, Figure 4 presents a sub-scene of HyMap data acquired on 3 June 1999 near Barrax, Spain, during ESA's DAISEX 1999 campaign (Digital Airborne Imaging Spectrometer Experiment, Müller and Hausold 2001). The HyMap sensor records 128 channels in the 400-2500 nm range and has a 61° field-of-view. Details of the instrument can be found in Cocks et al. (1998). The geographic coordinates of the scene are longitude –2.09° and latitude 39.08°. The flight altitude was 4 km above sea level and the ground elevation is 0.7 km. The scene was recorded at 11:54 UTC with a flight heading of 180°, a solar zenith angle of 17° and a solar azimuth angle of 170°. Ground reflectance measurements were performed with a FieldSpec FR spectroradiometer (FieldSpec 1997) and atmospheric measurements with a Licor 1800 sun photometer (LI-1800, 1992).

Figure 5 shows reflectance spectra of two selected fields (A=Alfalfa, and S2=soil) as indicated in Figure 4. The fields were recorded with a near-nadir geometry (scan angle < 10°). The dashed curves indicate the ground reflectance measurements resampled with the spectral channel response functions of HyMap. They were averaged over about 20 - 40 samples per field. The solid curves representing alfalfa and soil S2 indicate the corresponding spectra retrieved from the airborne instrument. The light-shaded areas indicate the plus/minus one standard deviation of the ground measurements. The dark-shaded vertical bars mark regions of strong atmospheric water vapour and CO_2 absorption. In the 1.8-1.95 µm region the HyMap instrument has no channels, so a straight line connects the wavelength gap of spectrometers 3 and 4. The deviation of ground measured reflectance and retrieved reflectance is up to 3% . The retrieved values are within the error margin of the ground measurements except for the HyMap channels with noise problems (below 0.45 µm) and the regions of strong water vapour absorption. For wavelengths beyond 2.4 µm, the noise level of the ground spectrometer instrument increases. A similar level of accuracy was obtained with other HyMap scenes acquired during several campaigns. These results were obtained for a variety of surface covers (soils, sand, asphalt, concrete, and dry and fresh vegetation) encompassing a very large reflectance range from 2 % to 70 % .

Put Fig 4 and Fig. 5 here

3.2 DAIS-7915 imagery of Timna, Israel, rugged terrain

As a sample case for rugged terrain under non-ideal conditions, a subimage of a DAIS-7915 scene of Timna (Israel) was selected. The DAIS sensor records imagery in 79 channels from the visible (0.5 µm) to the thermal (13 µm) spectrum with a 52° field-of-view. Details concerning the instrument are given by Strobl (1996). The geographic coordinates of the area are: longitude 34.9°, latitude 29.8°. The complete scene of flightline 1 (Timna north) contains about 3000 scan lines. It was acquired on 31 July 1997 between 9:33 and 9:37 h local time. The flight altitude was 3.650 km above sea level and the heading was 156°. The solar zenith and azimuth angles were 31.7° and 104.0°, respectively.

The scene was processed in the framework of a project of the German-Israeli Foundation. A digital elevation model of 25 m resolution (Hall 1996) was resampled to 5 m using bilinear interpolation to fit the ground sampling distance of the DAIS sensor. The mosaicked image of Figure 6 shows the DEM and related information (slope, aspect, sky view factor, and solar illumination). As a first processing step the parametric geocoding software PARGE (Schläpfer et al. 1998b, Meyer 1994, Schläpfer and Richter this issue) was used to calculate the ortho-rectified imagery. Information concerning the angular movements of the platform was taken from the DAIS gyros (roll, pitch, yaw) in combination with the low frequency aircraft (ARINC) gyros. GPS position data was recorded with a NovAtel system (NovAtel Communications Ltd. 1994). The information concerning the scan and azimuth angles for each pixel is calculated and stored in a PARGE / ATCOR4 interface file. Accordingly, the complete viewing and solar illumination geometry is known for each image pixel. Due to a partial lack of GPS clock information, the error of the ortho-rectification is in the range of 1-8 pixels for this scene.

Put Fig. 6 here

Figure 7 shows the results of the combined atmospheric / topographic correction. In many cases, the spatial resolution of the available DEM is not adequate to the sensor's pixel size. Therefore, regions of steep slopes and rapid slope or aspect changes are not adequately represented in the interpolated DEM. Large radiometric errors (over- or under-correction) can, therefore, be expected in those regions (Richter 1998). However, high spatial resolution DEMs of 1 – 5 m for airborne imagery are very expensive and often not available as in this case. An additional error source is the accuracy of the ortho-rectification as discussed in the first part of this paper. Nevertheless, for most regions of the image the topographic illumination influence is clearly reduced. Figure 8 demonstrates the reversal of brightness values in the spectral domain that is caused by the topographic effect: if a pixel is oriented towards the sun, the surface appears bright, and the reflectance spectrum without consideration of the topography (dashed line) lies above the spectrum that accounts for topography. If a pixel is oriented away from the sun, the surface appears darker. Therefore, the reflectance spectrum without consideration of the topography (dashed line) lies below the spectrum that accounts for the topography.

The elimination of topographic effects can also be shown with a statistical regression analysis. Figure 9 shows surface reflectance data (DAIS band 22 at 860 nm) of a transsect as a function of the local solar

the illumination angle (correlation coefficient 0.87), in the right part (combined atmospheric/topographic correction) the correlation coefficient (0.03) is strongly reduced indicating a successful removal of the topographic influence.

Put Figures 7 to 9 here

4. Accuracy of the method

There is not a single figure that can be given to summarize the accuracy for all situations, because the radiometric accuracy of the method depends on several factors: the calibration accuracy of the sensor, the quality of geometric co-registration of the spectral bands, the algorithm for ortho-rectification relying on auxiliary information such as attitude and GPS/DGPS, the accuracy of the radiative transfer code (MODTRAN 4), the correct choice of atmospheric input parameters, the terrain type (flat or rugged), and the surface cover.

Solar region:

In the solar region (wavelength < 2.5 µm), assuming a flat terrain, and avoiding the specular and backscattering regions, an accuracy of the retrieved surface reflectance of ±2% (for reflectance < 10%) and ±4% reflectance units (for reflectance > 40%) is possible as demonstrated in section 3.1. For rugged terrain, the most important parameter is an adequate spatial resolution of the DEM or DSM (digital surface model) and the exact ortho-rectification of the imagery. It would be desirable to have a DEM of a quarter of the sensor's spatial resolution or at least the resolution of the sensor's footprint which is seldom available (Richter 1998). Even in the latter case, errors in the matching of imagery and DEM can lead to large relative reflectance errors exceeding 100% for critical geometries (principal plane, e.g. a mountain ridge with half a pixel offset between imagery and DEM; Richter 1998). Thus, the non-availability of the required DEM resolutions of 1 – 10 m for airborne imagery in rugged terrain will limit the final accuracy of the geo-atmospheric image product in many cases.

For a flat terrain and larger off-nadir view angles, BRDF effects may have to be accounted for, and the appropriate surface-cover dependent BRDF model will influence the accuracy.

Thermal region:

In the thermal wavelength region beyond 8 µm, the surface temperature retrieval additionally depends on the correct choice of the surface emissivity. In the ATCOR 4 model the emissivity in *one* thermal band is based on a classification of the reflective bands if the sensor collects co-registered reflective and thermal band data. Depending on the surface cover classification (vegetation, soil, sand, asphalt, water, etc.), a typical emissivity value is assigned to each class (Salisbury and D'Aria 1992). If the deviation of the true surface emissivity to the assumed emissivity is less than 0.02 (a typical error margin), then the temperatures will be accurate to about 1-1.5 K. A rule of thumb is a surface temperature error of about 0.5-0.8 K per 0.01 emissivity error if the surface temperature is much higher than the boundary layer air

derived from the airborne DAIS-7915 instrument using the emissivity classification approach. These temperatures agreed well (1-2 K) with ground measurements (Coll et al. 2001).

5. Conclusions

A unified approach to parametric geocoding and atmospheric / topographic correction for airborne imagery has been developed. The model supports the geometries of most current airborne instruments including along-track (fore/aft) viewing sensors. Panchromatic, multispectral, and hyperspectral imagery from the solar spectral region and thermal region can be processed to obtain surface reflectance and temperature images. A large database may be used to avoid time-consuming runs with a radiative transfer code for cases that are already included in the database. Only a resampling with the channel-specific spectral response function of the selected instrument is required in these cases before processing the image data.

The method was successfully employed for the AVIRIS, HyMap and DAIS-7915 hyperspectral sensors in the framework of airborne NASA, ESA and national campaigns during 1998 to 2000. Good agreement of derived spectra (1-3 % reflectance) was obtained with simultaneous ground reflectance measurements in the near-nadir range and in flat terrain. For off-nadir angles larger than 10° bidirectional reflectance effects can play a role, leading to deviations from the nadir reflectance values. Therefore, a flexible BRDF interface has been provided to enable application-dependent corrections. For imagery in mountainous terrain the topographic illumination effect is strongly reduced with the proposed method even if the spatial resolution of an available DEM is often not sufficient.

A comparison of ground temperature measurements with surface temperature derived from the airborne DAIS-7915 spectrometer was conducted during ESA‘s DAISEX 1998/1999 campaign. The results show that an accuracy of 1-2 K can be achieved.

The method can be generalized to include wide field-of-view spaceborne sensors. The solar zenith angles at the image corners have then to be specified and bilinear interpolation can be applied to obtain the sun angle for each image pixel.

Acknowledgements: We thank the University of Valencia for the atmospheric data and the GeoForschungsZentrum Potsdam for the ground measurements performed during ESA's DAISEX'99 campaign. We are also grateful to the University of Tel-Aviv for the digital elevation model of the Timna area.

Appendix: radiative transfer equations

A) Basic equations

After running the series of required radiative transfer calculations and resampling with the sensor spectral response functions the radiance equation in the solar region for a cloud-free sky can be written as (Kaufman and Sendra 1988)

$$L = L_p + \tau_v \frac{\rho}{\pi} \frac{E_g(0)}{(1-\rho_r s)} \quad (1)$$

where

L at-sensor radiance for surface reflectance ρ ;

L_p path radiance ;

τ_{dir} direct (beam) transmittance ground-to-sensor;

τ_{dif} diffuse ground-to-sensor transmittance;

τ_v = τ_{dir} + τ_{dif} , total atmospheric transmittance;

E_{dir} direct solar flux on a horizontal surface;

E_{dif} diffuse solar flux on a horizontal surface;

E_g = E_{dir} + E_{dif} , $E_g(0)$ is calculated for a ground with ρ =0 ;

ρ_r large scale reference ground reflectance determining the effective global flux (ρ_r=0.15 is used here) ;

s spherical albedo of the atmosphere, accounts for atmospheric backscattering to the ground.

Since ρ and ρ_r are not known for image data and can vary within a scene, equation (1) has to be solved for ρ iteratively, compare equations (3, 7, 8). Equation (1) is calculated with the DISORT option (discrete ordinate radiative transfer) of MODTRAN4 using 8 streams (Stamnes et al. 1988, Berk et al. 1998) and reducing the large standard MODTRAN output to a smaller file containing only the terms L_p , τ_{dir} , τ_{dif} , E_{dir} , E_{dif} and s .

In the thermal spectral region (8-14 µm) the radiance equation can be written as (Kahle et al. 1980, Gillespie et al. 1998)

$$L = L_p + \tau_v \varepsilon L_{surf}(T) + \tau_v (1-\varepsilon) E_{th} / \pi \quad (2)$$

where

L at-sensor radiance ;

L_p thermal path radiance ;

τ_v ground-to-sensor atmospheric transmittance ;

ε surface emissivity ;

T surface temperature ;

L_{surf} blackbody radiance at the ground surface ;

E_{th} thermal downwelling flux on the ground.

The second term of equation (2) is emitted surface radiance reaching the sensor, the third term is the reflected surface radiance attenuated by the atmosphere. Equations (1-2) depend on wavelength, elevation,and scna angle. However, this dependence is omitted for brevity and the short notation for bandpass-resampled terms is employed, while the actual computer implementation is done as suggested in Richter (2000b).

B) Image-based atmospheric / topographic correction

The image-based atmospheric correction has to be performed iteratively employing the LUT's calculated previously. There are three major steps for the solar spectral region. The first step neglects the influence of the adjacency effect (Dave 1980) and can be written as (Richter 1998, 2000a):

$$\rho_{(i)}^{(1)}(x,y) = \frac{\pi \left[d^2 \{ c_0 + c_1 DN(x,y) \} - L_p(z,\theta_v,\phi) \right]}{\tau_v(z,\theta_v) \left[b(x,y)\, E_s \tau_s(z) \cos\beta(x,y) + E_{dif}^{*}(x,y,z) + E_g(z,\rho_r)\, \bar{\rho}_{terrain}^{(i)}\, V_{terrain}(x,y) \right]} \qquad (3)$$

where :

(i) iteration step (i=0, 1, 2, 3),

d sun-to-earth distance (astronomical units) ;

c_0 , c_1 offset and slope of linear radiometric calibration equation;

x, y horizontal coordinates, corresponding to the georeferenced pixel positions ;

z vertical coordinate, containing the elevation information from the DEM ;

DN(x,y) digital number of georeferenced pixel ;

θ_v view angle;

ϕ relative azimuth angle between sensor line-of-sight and solar azimuth,

$L_p(z,\theta_v,\phi)$ path radiance, dependent on elevation and geometry ;

$\tau_v(z,\theta_v)$ ground-to-sensor view angle transmittance, direct plus diffuse components ;

$\tau_s(z)$ Sun-to-ground beam (direct) transmittance ;

$\beta(x, y)$ angle between the solar ray and the surface normal (illumination angle) ;

b binary factor: b=1 if pixel receives direct solar beam, otherwise b=0 ;

E_s extraterrestrial solar irradiance ;

$E_d^*(x,y,z)$ diffuse solar flux on an inclined plane (see equation 5) ;

$E_g(z)$ global flux (direct plus diffuse solar flux on a horizontal surface at elevation z) ;

$\overline{\rho}_{terrain}^{(i)}$ average terrain reflectance within a 0.5 km radius (i=0, 1, 2, 3);

$\overline{\rho}_{terrain}^{(0)}$ initial value (constant for each band) of average terrain reflectance ;

$\overline{\rho}_{terrain}^{(i)}(x,y)$ locally varying average terrain reflectance, calculated iteratively (i=1,2,3) ;

$V_{terrain}(x,y)$ terrain view factor, range 0-1.

The term $E_s\,\tau_s(z)\cos\beta(x,y)$ represents the beam irradiance. It is preceded by a binary factor b(x,y), where b=1 if direct radiation illuminates pixel (x,y). The factor b is zero if $\cos\beta$ (x,y) < 0 , which means the pixel is completely in shadow and does not receive direct solar radiation. This applies for the case of self-shadowing. Factor b is also set to zero if shadow is cast from surrounding topography.

If $\theta_s, \theta_n, \phi_s, \phi_n$ denote solar zenith angle, terrain slope, solar azimuth and topographic azimuth, respectively, the illumination angle β can be obtained from the DEM slope and aspect angles and the solar geometry :

$$\cos\beta(x,y) = \cos\theta_s\cos\theta_n(x,y) + \sin\theta_s\sin\theta_n(x,y)\cos\{\phi_s - \phi_n(x,y)\} \qquad (4)$$

The diffuse solar flux on an inclined plane is calculated with Hay's model (Hay and McKay 1985):

$$E_d^*(x,y,z) = E_d(z)\left[b\,\tau_s(z)\cos\beta(x,y)/\cos\theta_s + \{1 - b\,\tau_s(z)\}V_{sky}(x,y)\right] \qquad (5)$$

The sky view factor can be computed from local information as $V_{sky}(x,y) = \cos^2(\theta_n(x,y)/2)$ based on the local DEM slope angle θ_n. The horizon algorithm provides a more accurate value of the sky view factor by considering the terrain neighborhood of each pixel (Dozier et al. 1981). V_{sky} and $V_{terrain}$ are related by :

$$V_{sky}(x,y) = 1 - V_{terrain}(x,y) \qquad (6)$$

The second step is the approximate correction of the adjacency effect caused by atmospheric crosstalk modifying the radiances of adjacent fields of different reflectances (Richter 1998) :

$$\rho^{(2)}(x,y) = \rho^{(1)}(x,y) + q\left(\rho^{(1)}(x,y) - \bar{\rho}(x,y)\right) \quad (7)$$

Here, $\bar{\rho}(x,y)$ is the low pass filtered image and q accounts for the strength of the adjacency effect. The third step is an enhancement to the previous paper (Richter 1998). It includes the spherical albedo effect on the global flux that was initially calculated with the reference reflectance ρ_r = 0.15 and is finally adapted to the scene-dependent value $\bar{\rho}$ by correcting with the difference $\bar{\rho} - \rho_r$:

$$\rho^{(3)}(x,y) = \rho^{(2)}(x,y)\left[1 - \left(\bar{\rho}(x,y) - \rho_r\right)s\right] \quad (8)$$

A second cycle of iterations of equations (3, 7, 8) using $\rho^{(3)}$ of equation (8) in equation (3) yields relative reflectance changes smaller than 1 % in most cases and can usually be omitted. A correction of bidirectional reflectance effects with empirical geometric functions has been discussed in Richter (1998). More elaborate image-based approaches employing the interface of Figure 3 will be presented in a separate paper.

A file interface to the parametric geocoding software PARGE (Schläpfer et al. 1998b, Schläpfer and Richter: this issue) for airborne sensors exists to obtain the pixel view and azimuth angles and to process geocoded imagery.

For thermal bands the at-sensor radiance was given in equation (2). Since surface emissivity ε and temperature are not known for image data equation (2) represents an underdetermined set of equations for the thermal channels. Several possibilities exist to address this problem (Kahle et al. 1980, Gillespie et al. 1998). Two options are currently implemented within the model ATCOR4 :

- ε = constant, specified by the user, and
- ε = $\varepsilon(x,y)$ where ε is determined from a spectral classification of the reflective bands using template reflectance spectra of vegetation, soils, asphalt, water, etc., to assign an emissivity class . This approach is feasible for instruments with coregistered reflective and thermal bands such as the hyperspectral DAIS-7915 sensor (Strobl et al. 1996). A detailed discussion is beyond the scope of this paper and can be found in Richter (2000a).

If ε has been selected or computed based on some assumptions, then the surface temperature T can then be calculated from the surface radiance using a second-order polynomial fit :

$$T = a_0 + a_1 L_{surf} + a_2 L_{surf}^2 \quad (9)$$

References

Berk, A., Bernstein, L. S., Anderson, G. P., Acharya, P. K., Robertson, D. C., Chetwynd, J. H., and Adler-Golden, S. M., 1998, MODTRAN cloud and multiple scattering upgrades with application to AVIRIS, *Remote Sensing of Environment* **65**, 367-375.

Borel, C. C., and Gerstl, S. A., 1994, Nonlinear spectral mixing models for vegetative and soil surfaces, *Remote Sensing of Environ*ment **47**, 403-416.

Bowker, D. E., Davis, R. E., Myrick, D. L., Stacy, K., and Jones, W. T., 1985, Spectral reflectances of natural targets for use in remote sensing studies, technical report, NASA reference publications 1139, Hampton, VA.

Cocks, T., Jenssen, R., Stewart, A., Wilson, I., and Shields, T., 1998, The HyMap airborne hyperspectral sensor: the system, calibration and performance, *First EARSeL Workshop on Imaging Spectroscopy, 6-8 Oct. 1998, Zurich, Switzerland*, pp. 37-42.

Coll, C., Richter, R., Sobrino, J. A., Nerry, F., Caselles, V., Jimenez, J. C., Labed-Nachbrand, J., Rubio, E., Soria, G., and Valor, E., 2001, A comparison of methods for surface temperature and emissivity estimation, In *Digital Airborne Imaging Spectrometer Experiment*, ESA Workshop Preliminary Proceedings WPP-182, ESA-ESTEC, Nordwijk, The Netherlands, (in press).

Diner, D. J., Bruegge, C. J. Martonchik, J. V., Bothwell, G. W., Danielson, E. D., Ford, V. G., Hovland, L. E., Jones, K. L., and White, M. L., 1991, A Multi-angle Imaging SpectroRadiometer for terrestrial remote sensing from the earth observing system, *Int. Journal of Imaging Systems and Technology* **3**, 92-107.

Dave, J. V., 1980, Effect of atmospheric conditions on remote sensing of a surface nonhomogeneity, *Photogr. Eng. Remote Sensing* **46**, 1173-1180.

Dozier, J., Bruno, J., and Downey, P., 1981, A faster solution to the horizon problem, *Computers & Geosciences* **7**, 145-151.

Duggin, M. J., and C. J. Robinove, C. J., 1990, Assumptions implicite in remote sensing data acquisiton and analysis, *Int. J. Remote Sensing* **11**, 1669-1694.

Fieldspec^{TM} 1997, User‘s Guide, Analytical Spectral Devices INC. Boulder, CO 80301-2333, USA.

Gao, B.-C., Goetz, A. F. H., Westwater, E. R., Conel, J. E., and Green, R. O., 1993, Possible near-IR channels for remote sensing precipitable water vapor from geostationary satellite platforms, *Journal of Applied Meteorology* **32**, 1791-1801.

Gillespie, A., Rokugawa, S., Matsunaga, T., Cothern, J. S., Hook, S., and Kahle, A. B., 1998, A temperature and emissivity separation algorithm for Advanced Spaceborne Thermal Emission and Reflection Radiometer (ASTER) images, *IEEE Trans. Geosc. Remote Sensing* **36**, 1113-1126.

Gower, J. F. R. Borstad, G. A., Anger, C. D., and Edel, H. R., 1992, CCD-based imaging spectroscopy for remote sensing: the FLI and CASI programs, *Canadian J. Remote Sensing* **18**, 199-208.

Green, R. O., 1992, Determination of the in-flight spectral and radiometric characteristics of the Airborne Visible/Infrared Imaging Spectrometer (AVIRIS), In *Imaging Spectroscopy: Fundamentals and Prospective Applications ,* edited by F. Toselli and J. Bodechtel (Kluwer Academic Publishers, London), pp.103-123.

Green, R. O., 1998, Spectral calibration requirements for Earth-looking imaging spectrometers in the solar-reflected spectrum, *Applied Optics* **37**, 683-690.

Hall, J. K., 1996, Digital topography and bathymetry of the area of the Dead Sea depression, *Tectonophysics* **266**, 177-185.

Hauber, E., Oberst, J., Flohrer, J., Sebastian, I., Zhang, W., Robinson, C., Jaumann, R., Neukum, G., 1996, The high resolution stereo camera (HRSC) for MARS 96: results of outdoor tests, *Int. Archives Photogr. Remote Sensing Vol. XXXI, Part B4, Commission IV, Vienna 1996,* pp. 349-354.

Hay, J. E., and McKay, D. C., 1985, Estimating solar irradiance on inclined surfaces: a review and assessment of methodologies, *Int. J. Solar Energy* **3**, 203-240.

Hu, B., Lucht, W., Li, X., and Strahler, A. H., 1997, Validation of kernel-driven models for global modeling of bidirectional reflectance, *Remote Sensing Environment*, **62**, 201-214.

Irons, J. R., Ranson, K. J., Irish, R. R., and Huezel, F. G., 1991, An off-nadir-pointing imaging spectroradiometer for terrestrial ecosystem studies, *IEEE Transactions on Geoscience and Remote Sensing* **GE-29**, 66-74.

Isaacs, R. G., Wang, W. C., and Goldenberg, S., 1987, Multiple scattering LOWTRAN and FASCODE models, *Applied Optics* **26**, 1272-1281.

Kahle, A. B., Madura, D. P., and Soha, J. M., 1980, Middle infrared multispectral aircraft scanner data analysis for geological applications, *Applied Optics* **19**, 2279-2290 (1980).

Kaufman, Y. J., and Sendra, C., 1988, Algorithm for automatic atmospheric corrections to visible and near-IR satellite imagery, *Int. J. Remote Sensing* **9**, 1357-1381.

Kaufmann, H., Meissner, D., Bodechtel, J., and Behr, F. J., 1989, Design of spectral and panchromatic bands for the German MOMS-02 sensor, *Photogrammetric Engineering and Remote Sensing* **55**, 875-881.

Kimes, D. S., 1983, Dynamics of directional reflectance factor distributions for vegetated canopies", *Applied Optics* **22**, 1364-137.

Kriebel, K. T., 1978, Measured spectral bidirectional reflection properties of four vegetated surfaces, *Applied Optics* **17**, 253-259.

Lee, T. Y., and Kaufman, Y. J., 1986, Non-Lambertian effects on remote sensing of surface reflectance and vegetation index, *IEEE Transactions on Geoscience and Remote Sensing* **GE-24**, 699-708.

LI-1800 Portable Spectroradiometer Instruction Manual, 1992 publication no. 8210-0030, LI-COR Inc., Lincoln, NE 68504, USA.

Meyer, P., 1994, A parametric approach for the geocoding of Airborne Visible/Infrared Imaging Spectrometer (AVIRIS) data in rugged terrain, *Remote Sensing Environm*ent **49**, 118-130.

Müller, A., and Hausold, A., 2001, The airborne imaging spectrometer acquisition progrogramme in 1998 and 1999, In: *Digital Airborne Imaging Spectrometer Experiment*, ESA Workshop Preliminary Proceedings WPP-182, ESA-ESTEC, Nordwijk, The Netherlands, (in press).

NovAtel Communications Ltd, 1994, GPSCard™ Command Descriptions Manual, Calgary, Alberta, Canada.

Proy, C., Tanre, D., and Deschamps, Y. P., 1989, Evaluation of topographic effects in remotely sensed data, *Remote Sensing of Environment* **30**, 21-32.

Richter., R., and Lehmann, F., 1989, MOMS-02 sensor simulation and spectral band selection, *Int. J. Remote Sensing* **10**, 1429-1435.

Richter, R., 1996, A spatially adaptive fast atmospheric correction algorithm*, Int. J. Remote Sensing* **17,** 1201-1214.

Richter, R.,.1997, On the in-flight absolute calibration of high spatial resolution spaceborne sensors using small ground targets, *Int. J. Remote Sensing* **18**, 2827-2833.

Richter, R., 1998, Correction of satellite imagery over mountainous terrain, *Applied Optics* **37**, 4004-4015.

Richter, R., and W. Lüdeker, W., 1999, Atmospheric water vapour derived from MOS-B land imagery, *Int. J. Remote Sensing* **20**, 1133-1140.

Richter, R., 2000a, Model ATCOR4: Atmospheric / topographic correction for wide FOV airborne imagery, report DLR-IB 564-04/00, Wessling, Germany.

Richter, R., 2000b, Bandpass resampling effects on the retrieval of radiance and surface reflectance, Applied Optics **39**, 5001-5005.

Richter, R., 2001, Atmospheric correction methodoloy for imaging spectrometer, In *Digital Airborne Imaging Spectrometer Experiment*, ESA Workshop Preliminary Proceedings WPP-182, ESA-ESTEC, Nordwijk, The Netherlands, (in press)

Roujean, J. L., Leroy, M., and Deschamps, P. Y., 1992, A bidirectional reflectance model of the earth's surface for the correction of remote sensing data, *J. Geophys. Research* **97**, 20 455-20468.

Salibury, J. W., and D'Aria, D. M., 1992, Emissivity of terrestrial materials in the 8 – 14 μm atmospheric window, *Remote Sensing of Environment* **42**, 83-106.

Sandmeier, S., and Itten, K. I., 1997, A physically-based model to correct atmospheric and illumination effects in optical satellite data of rugged terrain, *IEEE Trans. Geosc. Remote Sens.* **35**, 708-717.

Santer, R., Gu, X. F., Deuze, J. L., Devaux, C., Vermote, E., and Verbrugghe, M., 1992, SPOT Calibration at the La Crau Test Site (France), *Remote Sensing of Environment* **41**, 227-237.

Schläpfer, D., Borel, C. C., Keller, J., and Itten, K. I., 1998a, Atmospheric precorrected differential absorption technique to retrieve columnar water vapor, *Remote Sensing of Environment*, **65**, 353-366.

Schläpfer, D., Schaepman, M., and Itten, K. I., 1998b, PARGE: parametric geocoding based on GCP-calibrated auxiliary data, *SPIE Vol. 3438*, pp. 334-344, International Society for Optical Engineering, Washington, U.S.A.

Slater, P. N., 1980, Remote Sensing, Addison Wesley, Reading MA.

Slater, P. N., Biggar, S. F., Holm, R. G., Jackson, R. D., Mao, Y., Moran, M. S., Palmer, J. M., and Yuan, B., 1987, Reflectance and radiance-based methods for the in-flight absolute calibration of multispectral sensors, *Remote Sensing of Environment* **22**, 11-37.

Stamnes, K., Tsay, S.-C., Wiscombe, W., and Jayaweera, K., 1988., Numerically stable algorithm for discrete-ordinate-method radiative transfer in multiple scattering and emitting layered media, *Applied Optics* **27**, 2502-2509.

Strobl, P., Richter, R., Lehmann, F., Mueller, A., Zhukov, B., and Oertel, D., 1996, Preprocessing for the Digital Airborne Imaging Spectrometer DAIS 7915, SPIE Vol. **2758**, pp. 375-382, International Society for Optical Engineering, Washington, U.S.A.

Staenz, K., and Williams, D. J., 1997, Retrieval of surface reflectance from hyperspectral data using a look-up table approach, *Canadian J. Remote Sensing* **23**, 354-368.

Vane, G., Green, R. O., Chrien, T. G., Enmark, H. T., Hansen, E. G., and Porter, W. M., 1993, The airborne visible/infrared imaging spectrometer (AVIRIS), *Remote Sensing of Environment*, **44**, 127-143.

Vermote, E. F., Tanre, D., Deuze, J. L., Herman, M., and Morcrette, J. J., 1997, Second simulation of the satellite signal in the solar spectrum (6S): user guide version 2, July 1997, NASA Goddard Space Flight Center, Greenbelt, MD, USA.

Wan, Z., and Li, Z.-L., 1997, A physics-based algorithm for retrieving land-surface emissity and temperature from EOS/MODIS data, *IEEE Trans. on Geoscience and Remote Sensing* **35**, 980-996.

Wanner, W., Li, X., and Strahler, 1995, A. H., On the derivation of kernels for kernel-driven models of bidirectional reflectance, *J. Geophysical Research* **100** 21,077-21,089.

Wanner, W., Strahler, A. H., Hu, B., Lewis, P., Muller, J.-P., Li, X., Barker Schaaf, C. L., and Barnsley, M. J., 1997, Global retrieval of bidirectional reflectance and albedo over land from EOS MODIS and MISR data: theory and algorithm, *J. Geophys. Research* **102**, 17 143-17 162.

Wu, A., Li, Z., and Cihlar, J., 1995, Effects of land cover type and greenness on advanced very high resolution radiometer bidirectional reflectances: analysis and removal, *J. Geophysical Research* **100**, 9179-9192.

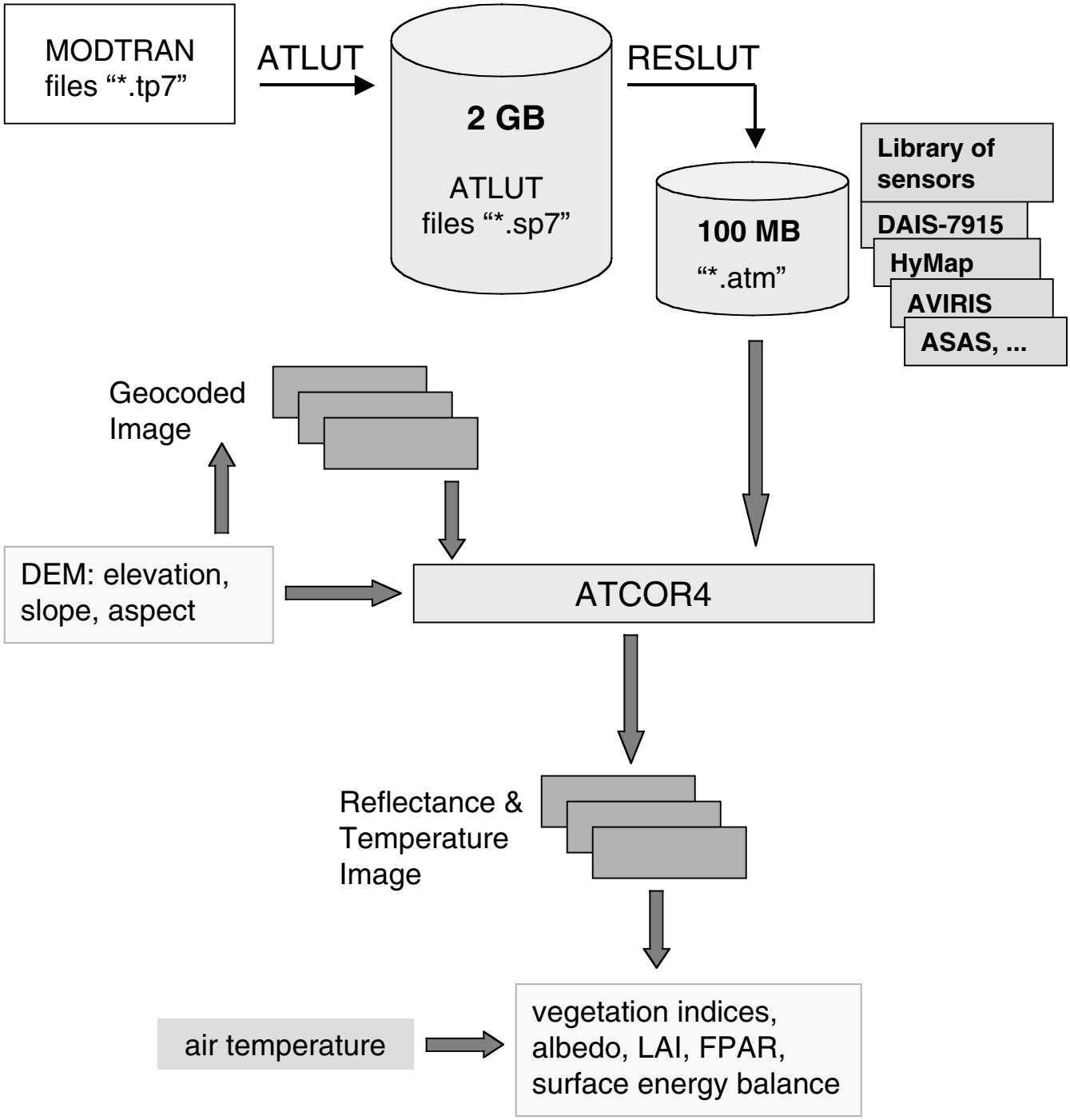

Figure 1. Block diagram of model ATCOR4.
(The acronyms are explained in the text).

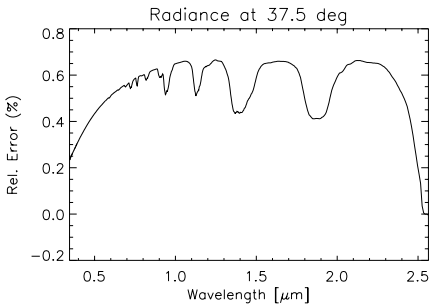

Figure 2. Relative error in scan angle interpolation related to the at-sensor radiance.
MODTRAN parameters: sensor at 4 km altitude, midlatitude summer atmosphere, rural aerosol, visibility 23 km, ground at sea level, water vapor column 2.36 g/cm^2 , solar zenith angle 60°, surface albedo 0%, and sensor view angles 35° and 40°. The relative at-sensor radiance error was calculated for the interpolated view angle 37.5° .

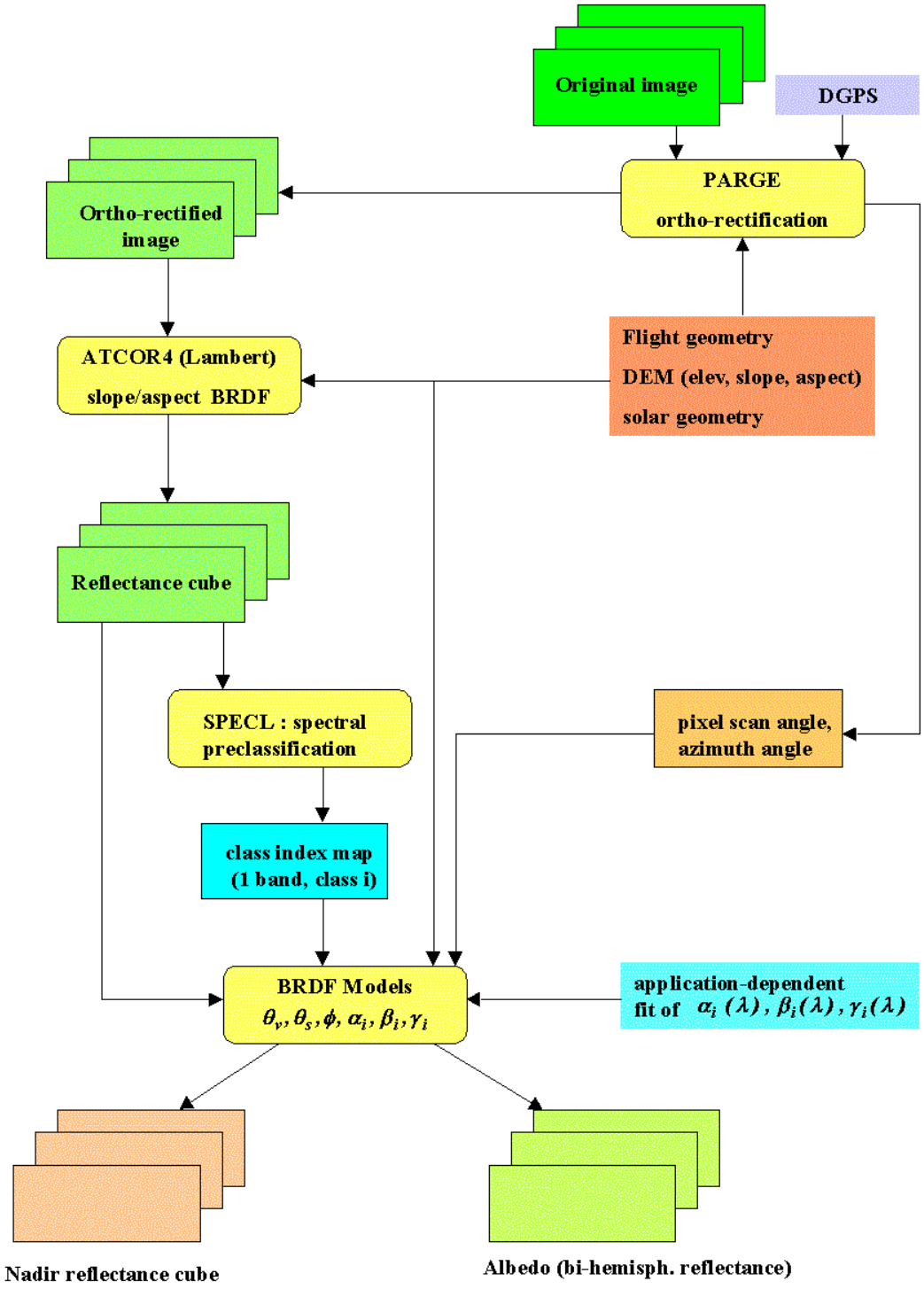

Figure 3. PARGE / ATCOR4 processing steps with BRDF interface.

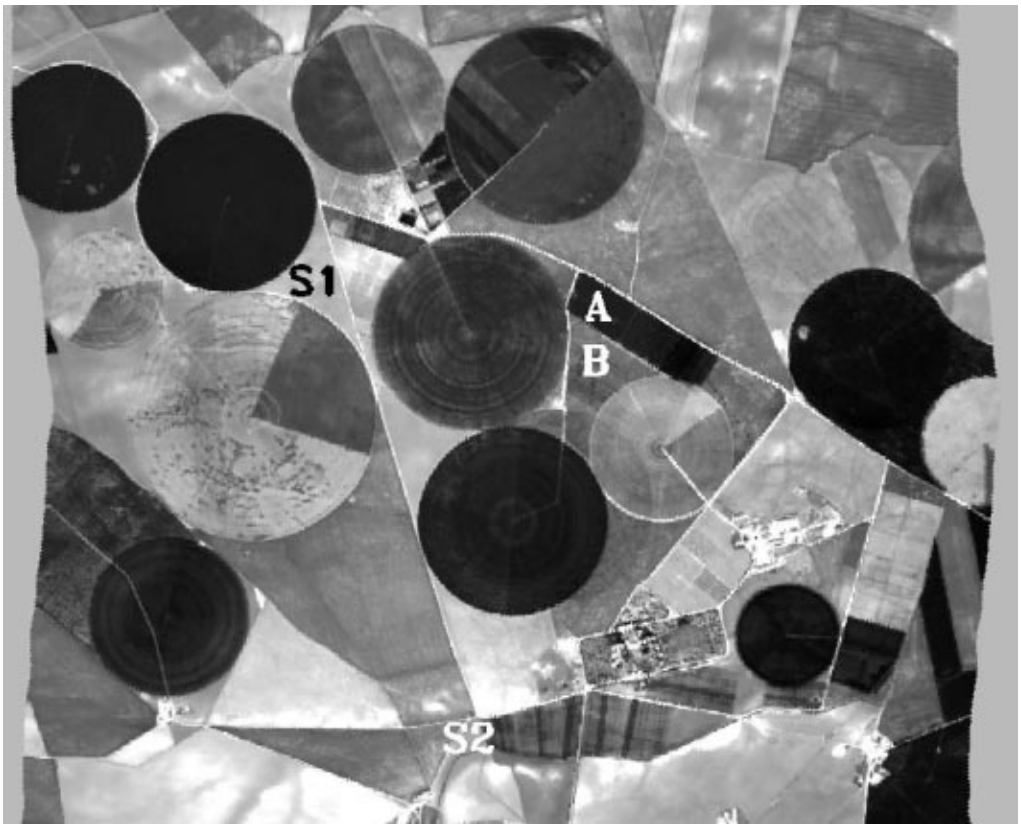

Figure 4. HyMap band 6 (503 nm) geocoded imagery of Barrax acquired 3 June, 1999. (A = Alfalfa, B = Barley, S1 and S2 are soil fields). The area covers 4.1 km × 3.3 km.

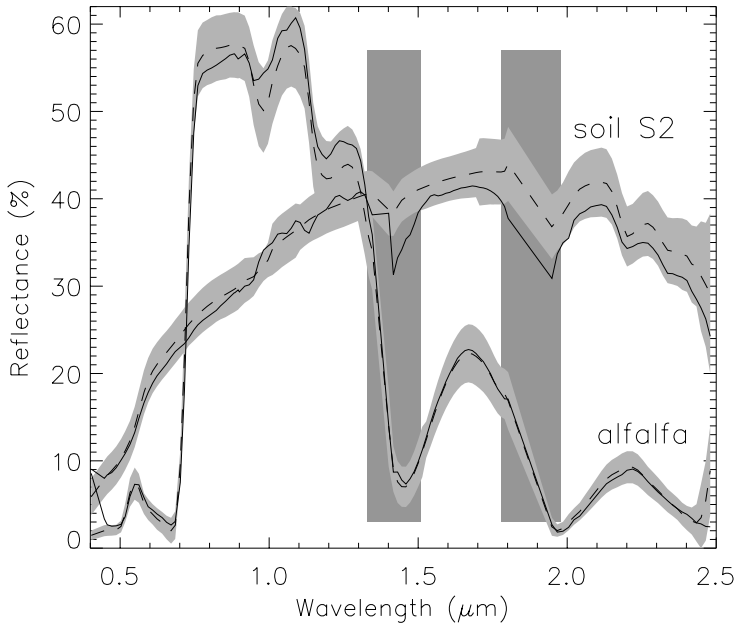

Figure 5. Comparison of ground-reflectance spectra of two surfaces with the corresponding HyMap reflectance spectra

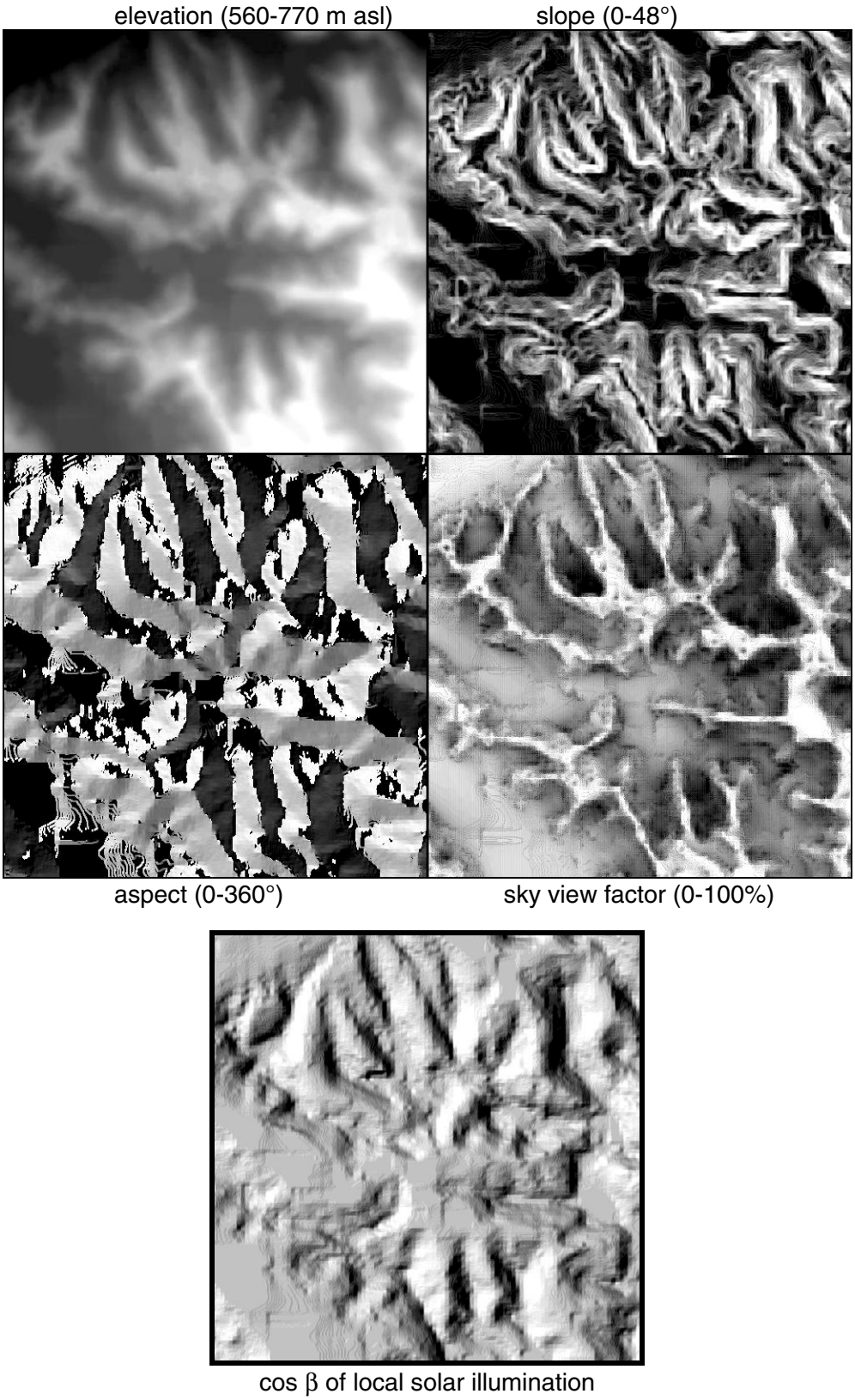

Figure 6. Mosaic of DEM related information.

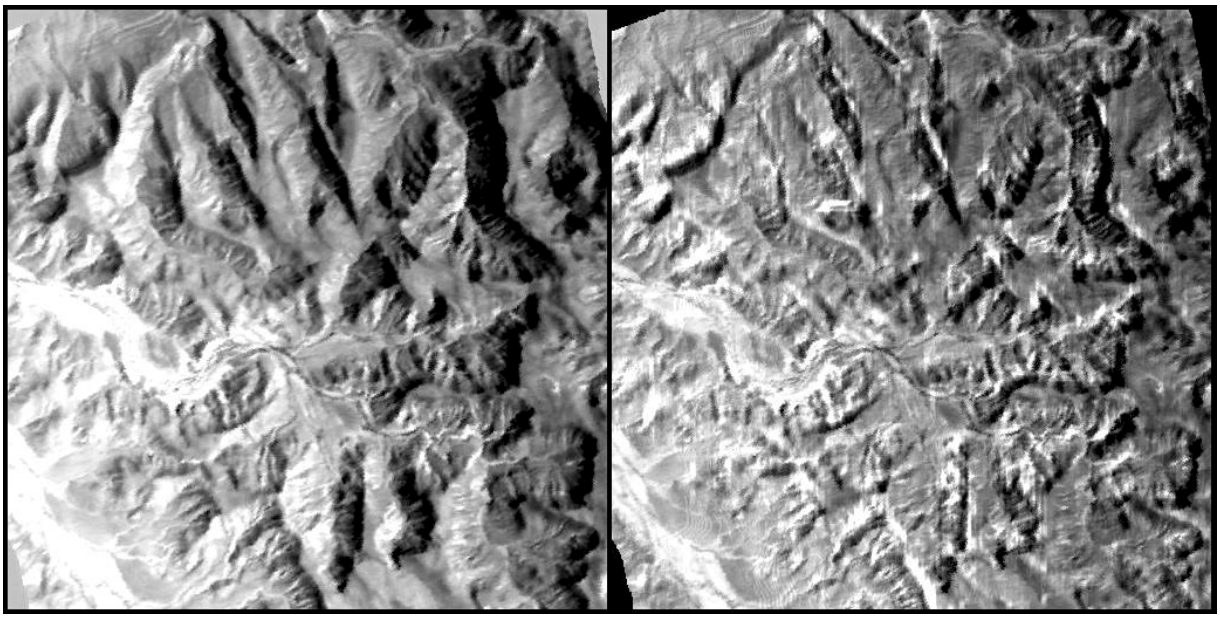

Figure 7. Original DAIS imagery (left) and after atmospheric / topographic correction (right). The image shows band 22 (860 nm) of DAIS.

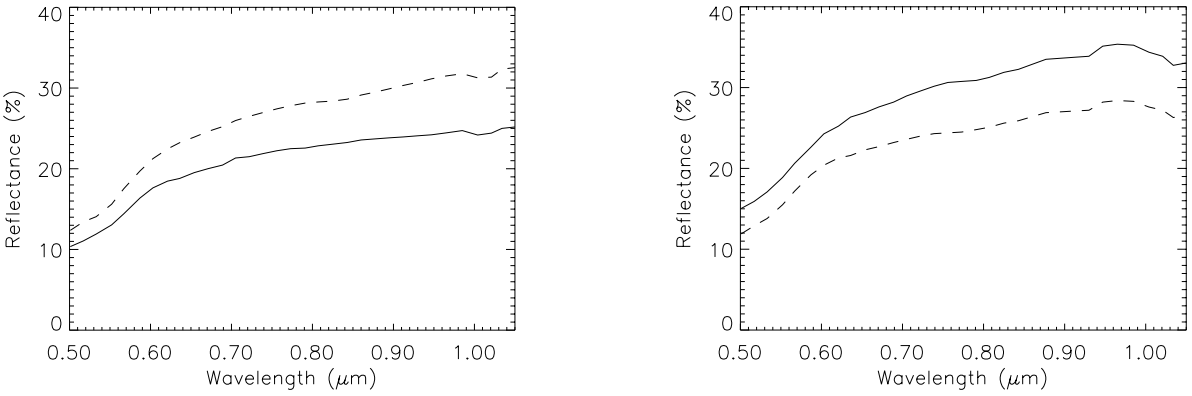

Figure 8. Pixel oriented towards the Sun on the left (slope 33°, aspect 143°, illumination angle 21°) and pixel oriented away from Sun on the right (slope 39°, aspect 214°, illumination angle 56°). The solid line represents reflectance spectra with atmospheric/ topographic correction, and the dashed line represents spectra with atmospheric correction only.

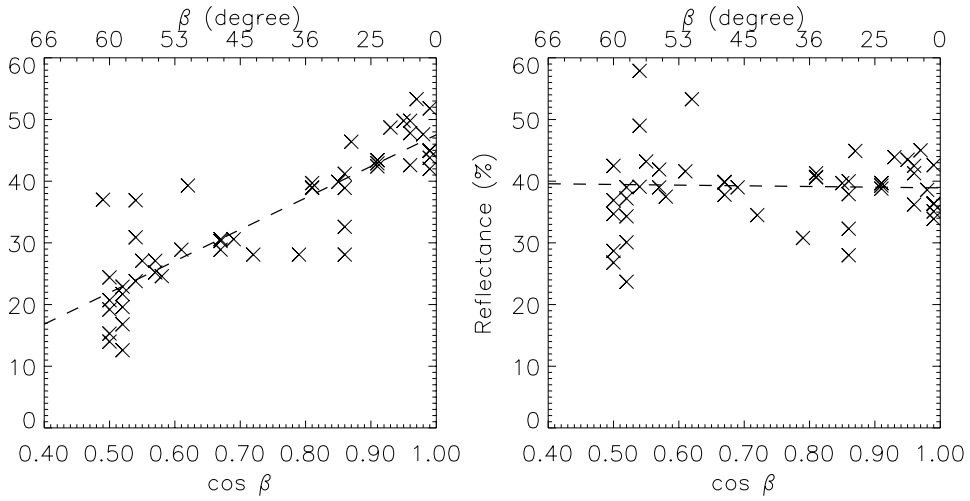

Figure 9. Regression analysis of an image transsect as a function of the solar illumination angle β using the DAIS band 22 at 860 nm.
The plot on the left depicts surface reflectance after atmospheric correction and the plot on the right represents surface reflectance after combined atmospheric / topographic correction.

Figure Captions

Figure 1. Block diagram of model ATCOR4.
(The acronyms are explained in the text).

Figure 2. Relative error in scan angle interpolation related to the at-sensor radiance.
MODTRAN parameters: sensor at 4 km altitude, midlatitude summer atmosphere, rural aerosol, visibility 23 km, ground at sea level, water vapor column 2.36 g/cm^2 .
Solar zenith angle 60°, surface albedo 0%, sensor view angles 35° and 40°, relative at-sensor radiance error calculated for the interpolated view angle 37.5° .

Figure 3. PARGE / ATCOR4 processing steps with BRDF interface.
Acronyms: BRDF=Bidirectional Reflectance Distribution Function; DGPS=Differential Global Positioning System, DEM = Digital Elevation Model.

Figure 4. HyMap band 6 (503 nm) geocoded imagery of Barrax acquired 3 June, 1999.
(A = Alfalfa, B = Barley, S1 and S2 are soil fields). The area covers 4.1 km $\times$ 3.3 km.

Figure 5. Comparison of ground-reflectance spectra of two surfaces with the corresponding HyMap reflectance spectra.

Figure 6. Mosaic of DEM related information.

Figure 7. Original DAIS imagery (left) and after atmospheric / topographic correction (right).
The image shows band 22 (860 nm) of DAIS.

Figure 8. Pixel oriented towards the Sun on the left (slope 33°, aspect 143°, illumination angle 21°) and pixel oriented away from Sun on the right (slope 39°, aspect 214°, illumination angle 56°).
The solid line represents reflectance spectra with atmospheric/ topographic correction, and the dashed line represents spectra with atmospheric correction only.

Figure 9. Regression analysis of an image transsect as a function of the solar illumination angle β using the DAIS band 22 at 860 nm.

The plot on the left depicts surface reflectance after atmospheric correction and the plot on the right represents surface reflectance after combined atmospheric / topographic correction.